OPEN ACCESS
International Journal of Neural Systems, Vol. 36, No. 5 (2026) 2650007 (16 pages)

DOI: 10.1142/S0129065726500073

World Scientific
www.worldscientific.com

Channel Graph Neural Network Revealing Multimodal Brain Connectivity Abnormalities in Schizophrenia

Jinnan Gong[*,†,‡,§,‖], Rui Ma[†,**], Roberto Rodriguez-Labrada[§,¶], Yanbing Zhu[*,‡,§], Hongrui Lin[*,‡,§], Yufan Zhou[*,‡,§], Yafeng Wang[*,‡,§], Dongrui Gao[*,†,‡,§], Dezhong Yao[*,‡,§], Sisi Jiang[*,‡,§] and Cheng Luo[*,‡,§,††]

[*]*The Clinical Hospital of Chengdu Brain Science Institute, University of Electronic Science and Technology of China, Chengdu 611731, P. R. China*

[†]*School of Computer Science, Chengdu University of Information Technology, Chengdu 610225, P. R. China*

[‡]*Research Unit of NeuroInformation, Chinese Academy of Medical Sciences, 2019RU035, Chengdu, P. R. China*

[§]*China-Cuba Belt and Road Joint Laboratory on Neurotechnology and Brain-Apparatus Communication, University of Electronic Science and Technology of China, Chengdu 610054, P. R. China*

[¶]*Cuban Neuroscience Center, La Habana, Cuba*

[‖]*18680807330@163.com*

[**]*marui_stitch@163.com*

[††]*chengluo@uestc.edu.cn*

Received 21 April 2025
Accepted 3 December 2025
Published Online 20 February 2026

Investigating abnormal brain network characteristics in schizophrenia can improve our understanding of disease mechanisms and help identify potential intervention targets. Graph learning techniques can capture high-dimensional features of large-scale brain networks and offer an inherent advantage for integrating multimodal data. To better integrate multimodal data and accurately localize network abnormalities associated with the disorder, this study proposes a channel-based graph neural network (C-GNN) model. First, node embedding of brain regions was constructed to capture structural connectivity patterns. Second, a branched attention module was introduced to adaptively identify important brain regions through channel attention. Finally, a graph feature-constraint module was developed to extract salient features by computing difference scores across feature channels. The C-GNN model achieved an accuracy of 84.37% in classifying individuals with schizophrenia. Interpretability analysis revealed key abnormal brain regions (e.g. orbital cortex, temporal fusiform cortex, lingual gyrus) and multimodal metrics (such as cortical thickness and ReHo)

[††]Corresponding author.

that contributed substantially to the classification. These findings offer insights into the underlying neural alterations in schizophrenia and may inform the development of targeted intervention strategies.

Keywords: Neuroimaging; multi-modality; biomarkers; graph neural network.

1. Introduction

Schizophrenia is a debilitating psychiatric condition characterized by brain network dysconnectivity,[1,2] affecting more than 20 million individuals worldwide. However, the underlying mechanisms of brain network alterations in schizophrenia remain unclear.[3] Identifying core features of large-scale brain network organization in patients may support the development of targeted nonpharmacological interventions.[4–6] Magnetic resonance imaging (MRI) has been widely used to examine changes in brain network topology in schizophrenia.[7,8] At the whole-brain level, reduced node centrality has been reported.[9] At the subnetwork level, key networks such as the default mode network (DMN)[10] and central executive network (CEN)[11] show impaired long-range connectivity.[12] Additionally, hub regions supporting major fiber pathways differ significantly between patients and healthy controls (HC).[13] Together, these findings indicate multi-level brain network abnormalities associated with schizophrenia.

Conventional connectome analyses mainly focus on network topology while overlooking intrinsic node (brain region) properties. Deep graph neural networks (GNNs)[14] enable learning of node embeddings and extraction of higher-order features, offering a more comprehensive means of characterizing brain network alterations. For example, Chen *et al.* used sparse brain graphs modeled from functional magnetic resonance imaging (fMRI) as input and proposed a novel Sparse Feature Combination GNN to identify brain regions crucial for classification, thereby pinpointing all areas associated with brain diseases.[3] Zheng *et al.* developed an interpretable GNN using prototype learning to analyze fMRI, effectively distinguish psychotic patients from HC and identify biologically meaningful subtypes.[15] Thapaliya' and Zeng's work established GNNs as a powerful paradigm for decoding individual cognitive differences from rsfMRI.[16,17]

Despite these advances, several challenges remain. First, different MRI modalities capture distinct attributes — dynamic signals from fMRI, anatomical features from sMRI, and microstructural information from dMRI[18,19] — and effective multimodal integration is needed to enhance GNN performance. Second, regarding the construction of edge features, functional connectivity is time-dependent and includes negative connections, whereas dMRI-based white matter connectivity lacks stability when constructing long-range tracts[20,21]; thus, more robust edge construction strategies are required. Third, given the high dimensionality of MRI data, efficient identification of critical diseaserelated features remains essential.

To address these issues, this study proposes a channelbased GNN (CGNN) that integrates multimodal MRI features and incorporates a channel attention mechanism for schizophrenia classification and feature localization. Specifically, FOCA,[22] FCD[23] and *et al.* from fMRI; cortical thickness and gray matter volume (GMV)[24] from sMRI; and white matter connectivity from dMRI tractography,[25] are used for graph construction. A graph embedding method is applied to capture highorder topological features of the white matter network. A branch attention network (BAN) module and a graph feature constraint (GFC) module are then used to identify key nodes and select salient features. Finally, the high-weight regions and features identified by the CGNN are visualized to provide insights into the potential pathological mechanisms of schizophrenia.

2. Methods

2.1. *Participants*

Seventy schizophrenia patients diagnosed based on the Diagnostic and Statistical Manual of Mental Disorders, fourth edition (DSM-IV), structured clinical interview,[26] were recruited from both inpatient and outpatient settings. Clinical, psychological, behavioral, and MRI data were collected from all the patients. Additionally, 73 age-and-gender-matched subjects were recruited as the HC group with MRI

Table 1. Description of study sample.

	Patients (mean/standard deviation)	HC (mean/standard deviation)
Number of subjects	70	73
Gender (male/female)	51/19	39/34
Years of education	11.58/2.75	10.69/3.23
Age	40.82/11.25	38.68/9.64
Age range	16–66	19–56
Duration of illness	15.82/10.62	—
Positive score	12.88/5.73	—
Negative score	21.1/6.56	—
Total score	28.1/6.10	—

data collected. Neuroimaging data were gathered by using a 3 T MRI scanner (GE Discovery MR 750, USA). During a semi-structured interview, each patient underwent assessment of psychotic symptoms using the Positive and Negative Syndrome Scale (PANSS).[27] At the time of the study, all participants were receiving medication.[28] Table 1 shows the demographic information of all participants.

2.2. *Data acquisition parameters*

Anatomical MRI acquisition: The fast spoiled gradient echo (FSPGR) three-dimensional T1-weighted (3D-T1) sequence was employed to acquire high-resolution anatomical, structural images with repetition time (TR)/echo time (TE) = 6.008 ms/1.984 ms, flip angle = 9°, matrix size =256 × 256, isotropic voxel size = 1 mm, axial acquisition, and whole-brain coverage in 152 slices with slice thickness = 1 mm.

Resting-state fMRI (rsfMRI) acquisition: rsfMRI images were acquired with participants lying quietly with eyes closed. The imaging was performed with a standard T2*-weighted echo-planar imaging (EPI) sequence, where TR/TE = 2000 ms/30 ms, flip angle = 90°, FOV = 24 × 24 cm, matrix size = 64 × 64, and 35 contiguous axial slices covering the entire brain. Each subject underwent 255 consecutive time points of whole-brain scanning, totaling 8 min and 30 s of scan duration. To enhance data reliability, two sets of rsfMRI images were acquired for each subject.

dMRI Acquisition: dMRI data were collected in two parts using diffusion-weighted spin echo EPI sequences. The primary data included three nondiffusion-weighted images and 64 diffusion-weighted images with specific parameters: b-value = 1000 s/mm^2, TR = 8500 ms, frequency encoding direction = left/right, matrix size = 128 × 128, FOV = 25.6 × 25.6 cm, slice thickness = 2 mm, covering the whole brain with 78 contiguous slices. Besides, the second part of dMRI data consisted of 6 diffusion-weighted images with frequency encoding direction = anterior/posterior. The second part of dMRI data will be used to estimate magnetic susceptibility and minimize image distortion effects caused by susceptibility (by using EDDY toolbox of FSL).

2.3. *C-GNN model*

The framework of the C-GNN model is illustrated in Fig. 1. The methodology encompasses the extraction of node and edge features, graph construction description, a BAN, and a graph constraint module.

2.3.1. *Graph construction*

After MRI preprocessing (see Appendix: Data Preprocessing (Table A.1)), the brain was parcellated into 96 regions based on the Harvard–Oxford cortical atlas. Each region was treated as a node in the graph, with its neuroimaging attributes extracted as node features. Embeddings representing white matter connectivity between regions were used as edges.

Node features were extracted from fMRI and sMRI. Functional features included amplitude of low-frequency fluctuations (ALFF)/fractional amplitude of low-frequency fluctuations (fALFF) and regional homogeneity (ReHo), calculated using REST[29]; as well as FOCA, local FCD, global FCD and long-range FCD obtained using NIT.[30] Structural features included cortical thickness, GMV, and white matter volume (WMV), extracted using FreeSurfer[31] and SPM.[32]

After preprocessing of dMRI, probabilistic tractography (permutation for 10,000 times per seed voxel) was conducted to estimate fiber connectivity between brain regions. In this step, distance correction was applied to account for the decline in connectivity probability with increasing distance from the seed mask. After tractography, white matter connectivity matrices were computed by the average

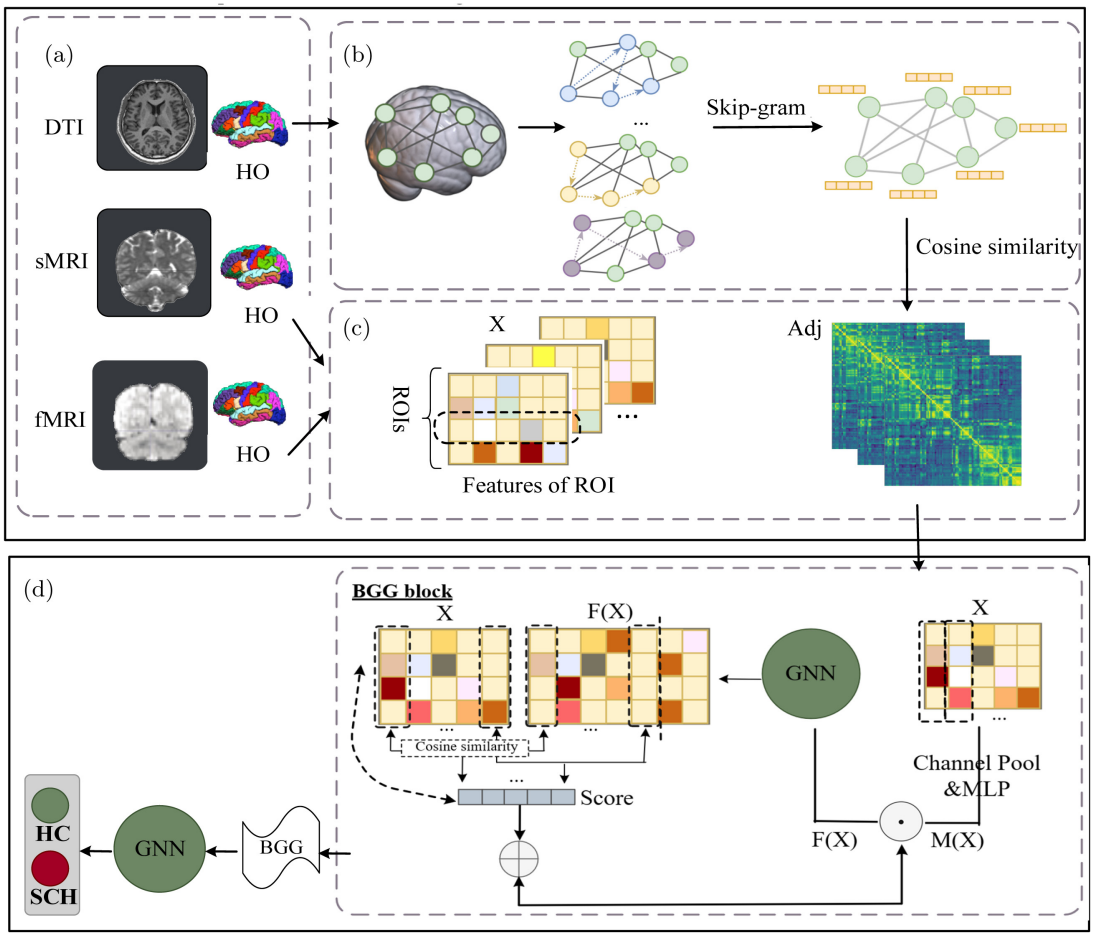

Fig. 1. Schematic diagram of the proposed CGNN model for binary classification of schizophrenia. Multimodal features are extracted from sMRI and fMRI, and structural connectivity is obtained from DTI (a). Graph edges are constructed using the Node2vec embedding module (b). The resulting feature matrix and new adjacency matrix are shown (c). The model then performs feature learning and completes the final classification task (d). The featurelearning component contains two BGG modules and one GNN module. Each BGG module includes a branch attention network (BAN) for identifying salient brain regions, a graph feature constraint (GFC) module for selecting salient features, and a GNN module. The final output consists of two classification categories.

white matter connectivity strength between each pair of regions.

To characterize interregional relationships and infer potential missing connections in the structural connectivity matrix, the node2vec graph embedding method was applied. This approach produced low-dimensional vector representations of brain regions to better capture their underlying structural associations.[33]

First, each subject's white matter connectivity matrix $C_{ij} \in R^{n*n}$ (where C_{ij} represents the connection strength between node i and node j, and n denotes the number of brain region nodes) was employed as the input.

Only the 10 strongest edges for each brain region node were retained, with the weights of the other edges set to zero, so that a strongly connected subgraph $G \in R^{n*n}$, as shown as follows:

$$G_{ij} = \begin{cases} C_{ij}, & C_{ij} \in T_i, \\ 0 & \text{otherwise}, \end{cases} \tag{1}$$

$$T_i = \{x \in E_i \,|\, \text{rank}(x) \leq \min(10, |E_i|)\}. \tag{2}$$

In these equations, T_i represents the set of the top 10 edge weights for node i, and $\text{rank}(x)$ denotes the ranking of element x within the edge set E_i of the original structural connectivity matrix C_{ij} when sorted in descending order.

Subsequently, a strategy-based random walk sampling was performed on graph G, and multiple random walks were executed for each node to generate node sequences. The random walk process was controlled by parameters p and q to balance between breadth-first search (BFS)[34] and depth-first search (DFS).[35] Furthermore, node pairs were extracted from the generated node sequences by treating the nodes within each context window as context nodes for the corresponding target node, thereby yielding a large number of node pairs. Finally, the skip-gram model was utilized to optimize the node embedding vectors,[36] with the objective of reducing the distance between adjacent nodes in the embedding space. After these steps, each node was represented as a vector v, and the cosine similarity among these node vectors was calculated to obtain the graph's adjacency matrix $A_{ij} \in R^{n*n}$, as shown as follows:

$$A_{ij} = \cos(v_i, v_j) = \frac{v_i \cdot v_j}{\|v_i\| \cdot \|v_j\|}. \tag{3}$$

At this point, we have accomplished the multimodal MRI-based graph construction workflow: regional measurements from fMRI and sMRI function as node features, with white matter connectivity between regions, embedded via the node2vec approach, serving as edges.

2.3.2. *Branch attention network module*

The channel attention mechanism[37] was first proposed in the field of computer vision.[38,39] The squeeze-and-excitation block was proposed, and this block dynamically adjusted channel-specific feature responses through explicit modeling. In this module, we designed a BAN module based on network-wise attention[40] and SENet,[41] as presented in Fig. 2. And applied the channel-wise attention mechanism to graph data to strengthen the effectiveness of node features.

First, the feature matrix X was processed using channel-wise max pooling and mean pooling to extract $X_{\max} \in R^{n*1}$ and $X_{\text{ave}} \in R^{n*1}$.

Second, the results obtained by the two pooling methods were provided as input to MLP1 and MLP2, respectively. SENet's excitation module was used in MLP, which includes two full connection (FC) operations and one activation function operation to achieve cross-channel learning of features.[42,43] MLP1 and MLP2 output $X'_{\max}$ and X'_{ave} respectively, as shown below:

$$X'_{\max} = W_{2,\max} \cdot \text{relu}(W_{1,\max} \cdot X_{\max}), \tag{4}$$

$$X'_{\text{ave}} = W_{2,\text{ave}} \cdot \text{relu}(W_{1,\text{ave}} \cdot X_{\text{ave}}), \tag{5}$$

where $W_{1,\max}$, $W_{1,\text{ave}}$,$W_{2,\max}$, and $W_{2,\text{ave}}$ are weight matrices of the FC layer.

Finally, the two outputs were added and summed element by element, the information obtained by two different channel learning methods was fused, and the activation function was used to convert it into an attention score $M(X) \in R^{n*1}$, as shown as follows:

$$M(X) = \text{Sigmoid}(X'_{\max} \oplus X'_{\text{ave}}). \tag{6}$$

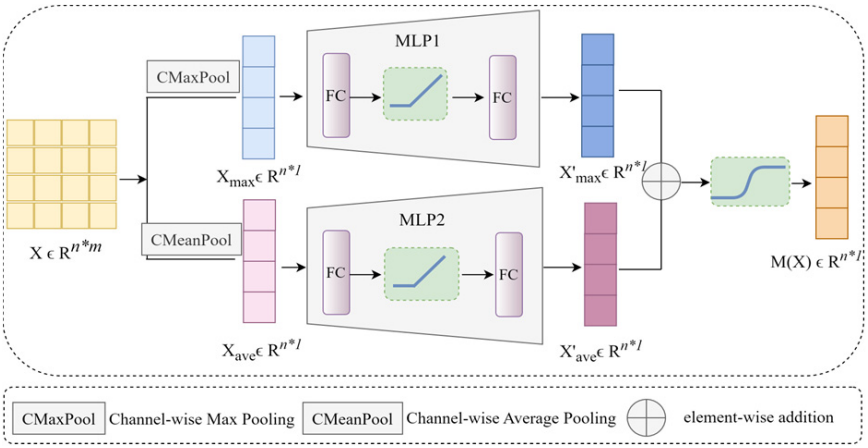

Fig. 2. Architecture diagram of the BAN module. The multimodal feature matrix $X \epsilon R^{n*m}$ is used as the input, where n represents the number of ROIs, and m corresponds to the number of features (X represents multimodal neuroimaging features, which are treated as channels in this module).

The branch attention score $M(X)$ calculated above is used to adaptively adjust each node of the input feature matrix. Specifically, these attention scores are applied to the output features of the GNN module through element-wise multiplication, thereby better capturing the weight of node features in the graph convolution operation. Among them, the GNN module is implemented using spatial graph convolution, as shown as follows:

$$F(X) = \mathrm{GNN}(A, X) = \mathrm{relu}(\mathrm{BN}(\tilde{D}^{-\frac{1}{2}}\mathrm{A}\tilde{D}^{-\frac{1}{2}}XW)), \tag{7}$$

$$S(X) = M(X) \odot F(X), \tag{8}$$

where A represents the adjacency matrix obtained after graph embedding learning, D represents the degree matrix, W is the weight matrix, BN is batch normalization, and $F(X)$ is the feature representation obtained by the GNN module.

2.3.3. *Graph feature constraint*

This section proposes a method for feature channel differentiation scoring. By calculating the feature channel differentiation score and weighted learning of different feature channels based on this score, important features that contribute to the model were obtained.

First, we calculated the cosine similarity between the convolutional features of the GNN module and the original features. Since the dimensions of $F(X)$ and X were different, we ensured that they were consistent before calculating the cosine similarity. In this experiment, we used the channel cropping alignment method to achieve this. Let $F(X) \in R^{n*d_1}$ denote the convolved feature of the GNN module, where $d_1 > m$. The channels of $F(X)$ were partitioned, and the first $m$channels were selected to form $F_{\mathrm{cut}}(X) \in R^{n\times m}$. For the j channel ($j = 1, 2, 3, \ldots, m$), the cosine similarity score s_j was calculated as follows:

$$\begin{aligned}&\mathrm{cosine}\big(X :, _j, F_{\mathrm{cut}}(X) :, _j\big)\\ &\quad = s_j = \frac{\sum_{i=1}^{n} X_{ij} \cdot F_{\mathrm{cut}}(X)_{ij}}{\sqrt{\sum_{i=1}^{n} X_{ij}^2} \cdot \sqrt{\sum_{i=1}^{n} F_{\mathrm{cut}}(X)_{ij}^2}},\end{aligned} \tag{9}$$

where X_{ij} represents the element in the ith row and jth column of the original feature matrix X, and $F_{\mathrm{cut}}(X)_{ij}$ represents the corresponding element in the sliced convolution feature matrix $F_{\mathrm{cut}}(X)$.

Subsequently, the obtained cosine similarity was used to calculate the difference score among the feature channels as follows:

$$\mathrm{Score} = 1 - \mathrm{Nor}(\mathrm{cosine}(X, F(X))), \tag{10}$$

where Nor denotes the normalization operation, which constrains the cosine similarity results within the range [0,1]. The score represents the differentiation score.

Finally, based on the differentiation scores, we filtered the information of the original input feature channels by element-wise multiplying the differentiation scores with the original input feature channels, achieving weighted learning of important features, as follows:

$$Z(X) = \mathrm{Score} \odot X, \tag{11}$$

where X is the original input feature channels, Score represents the differentiation scores, and $\odot$ indicates the Hadamard product (element-wise multiplication).

Then, the output of the GFC module was element-wise added to the output of the BAN module to obtain the final result of the BGG module, as demonstrated below:

$$H = S(X) \oplus Z(X). \tag{12}$$

After two layers of BGG module learning and one layer of GNN module, a total of three layers of learning, the output was then passed via global average pooling and an FC layer, and finally, the classification result was obtained via the activation function and the cross-entropy loss function was used for the binary classification task, as shown below:

$$\tilde{y} = \mathrm{Sigmoid}(\mathrm{FC}(\mathrm{GavgPool}(\mathrm{GNN}(H^{(2)})))), \tag{13}$$

$$L(y, \tilde{y}) = -(y \cdot \log(\tilde{y}) + (1 - y) \cdot \log(1 - \tilde{y})), \tag{14}$$

where $H^{(2)}$ is the output of two BGG layers, and GavgPool averages node features to generate a graph-level embedding.

2.4. *Experimental settings*

In the graph embedding method, we employed the policywalk mechanism, where the walk length was set to 20, the number of walks was set to 10, and hyperparameters p and q were set to 1 and 0.25, respectively. For node embedding using the skipgram approach, the context window size was set to 8, and

the number of iterations was fixed at 3. For the binary classification task, 78% of the data was used for training and 22% for testing. The learning rate was set to 0.0000085, and the batch size to 32. We used the Adamax optimizer, which adaptively adjusts the learning rate to facilitate more efficient convergence toward the global minimum.

To avoid parameter redundancy, we employed three graph convolutional layers and limited the number of hidden units in each layer to fewer than 64. Ten multimodal brain imaging metrics (structural MRI and functional fMRI) were selected as feature inputs to reduce redundant information. Batch normalization was applied after each convolutional layer to stabilize gradients, and dropout was incorporated to further enhance generalization. $L2$ regularization was also used to prevent overfitting.

To provide a comprehensive explanation of the selected hyperparameters, the related experiments are presented in the Appendix (Table A.2). The experiments were conducted on a personal computer equipped with a 13th Gen Intel Core i9-13900HX CPU (2.20 GHz), 16 GB of memory, and a GeForce RTX 4060 GPU. Model training and testing were performed on the open-source PyTorch 1.11 framework with torch-geometric 2.4.0.

2.5. *Interpretability analysis*

In addition to classifying schizophrenia based on large-scale network features, this study also aimed to identify key abnormal brain regions and features in patients. Therefore, after model training, we performed visualization and interpretability analyses to further highlight the model's potential clinical applicability.

2.5.1. *Extraction of significant brain areas*

To demonstrate the interpretability of the model, we applied the UGradCAM[44] visualization technique, which integrates gradient and feature information to estimate the contribution weight of each brainregion node to the model output. To ensure the reliability of the identified regions, the model was trained 10 times. From each training, the top 10 regions with the highest contributions were recorded. These regions were then ranked by their frequency of occurrence across all runs, and the 10 most frequently appearing regions were identified as significant brain areas.

2.5.2. *Statistical analysis of regional features*

To further identify brain features that substantially influence the model and may hold research value, we applied a gradientguided interpretability method, Saliency Map,[45] after model training, to evaluate the sensitivity of input features and visualize their contributions to the classification task. After regressing out confounds such as age and gender, we used the nonparametric Mann–Whitney U-test to assess group differences in the significant brain features associated with schizophrenia.

2.5.3. *Prediction of symptom severity*

To further validate the association between the key brain regions and clinical symptoms, and to explore their potential links to schizophrenia symptomatology, we constructed a symptomseverity prediction model. A Chebyshev[46] graph network was used to extract features from the ten key brain regions, with the four core PANSS symptom domains (positive, negative, general psychopathology) serving as regression targets. The model was trained to predict symptom severity for each participant, and the Pearson correlation coefficient was used to evaluate the relationship between the predicted and actual scores.

3. Results

3.1. *Overall classification performance of the model*

The overall performance of the model is demonstrated in Table 2. Metrics, including accuracy, sensitivity, specificity, $F1$-score, and area under the curve (AUC), were calculated and compared with those of other GNN methods. The proposed model achieved the best performance among all evaluated methods.

3.2. *Ablation study*

The effectiveness of the white matter network embedding (Node2vec), BAN module, and GFC

Table 2. Performance comparison between the proposed CGNN model and other GNN algorithms.

Model	Acc (%)	Sen (%)	Spe (%)	$F1$ (%)	AUC (%)
MLP[47]	72.66 ± 3.0	72.92 ± 3.2	63.75 ± 4.5	72.72 ± 3.5	71.88 ± 3.0
GCN[48]	75.39 ± 2.6	76.04 ± 3.9	74.73 ± 5.3	75.49 ± 3.7	74.39 ± 2.9
GAT[49]	73.96 ± 3.0	75.00 ± 3.5	73.62 ± 4.0	72.79 ± 3.8	74.22 ± 2.8
Chebynet[46]	74.48 ± 2.8	74.38 ± 3.2	71.25 ± 4.2	74.15 ± 3.5	72.66 ± 3.0
GraphSAGE[50]	74.37 ± 3.2	75.78 ± 3.7	65.00 ± 5.0	74.75 ± 4.0	73.44 ± 3.2
SGCN[51]	73.75 ± 3.5	74.22 ± 3.8	66.25 ± 5.2	73.59 ± 4.1	71.87 ± 3.5
Graph-Unet[52]	75.00 ± 2.7	75.52 ± 3.0	79.76 ± 3.5	78.30 ± 3.2	75.95 ± 2.8
DeeperGCN[53]	71.88 ± 3.8	72.58 ± 3.5	66.25 ± 4.8	72.44 ± 4.0	71.86 ± 3.7
GCNII[54]	74.38 ± 2.9	75.32 ± 3.2	81.25 ± 3.6	75.46 ± 3.5	74.38 ± 2.9
EGC[55]	80.62 ± 2.5	80.94 ± 2.8	75.00 ± 3.5	80.64 ± 3.0	80.00 ± 2.5
Ours	**84.38 ± 2.3**	**87.50 ± 2.9**	**78.75 ± 3.6**	**85.71 ± 2.3**	**83.10 ± 3.1**

Note: The bold values represent the proposed model achieved the best performance among all evaluated methods.

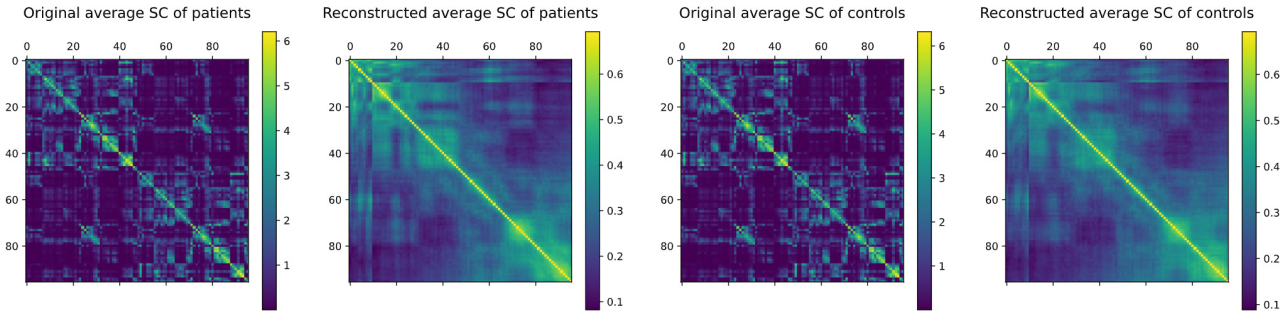

Fig. 3. Visualization of the original structural connectivity and the structural connectivity after graph embedding learning.

module was evaluated through ablation experiments. The results of these ablation studies are presented in Tables 3–5.

In the first comparison, the embedded connectome generated by the Node2vec method was replaced with the original whitematter connectome as the graph's edge features (Fig. 3). As demonstrated in Table 3, the proposed C-GNN achieved the best classification performance when the embedded white matter matrix was used as an edge feature, indicating that network embedding helps enhance the reliability of whitematter connectivity by capturing global topological properties.

The performance of the branch attention module is reported in Table 4. When channel attention was applied to weight feature channels, the model exhibited improvements across all performance metrics.

The performance evaluation of the GFC module is presented in Table 5. Several channel-alignment strategies were compared. "Cor" represents cropping feature channels to align their dimensions; "Fc" represents dimensionality reduction through linear transformation; "Inter" represented increasing channel dimensions using linear interpolation; "C" denotes computing cosine similarity across feature

Table 3. Ablation study results for the network embedding method.

Module	Acc	Sen	Spe	$F1$	AUC
GNN	73.126	73.178	58.750	72.564	72.884
GNN+ network embedding	79.234	79.390	67.500	79.094	78.078

Table 4. Ablation study results for the BAN module.

Module	Acc	Sen	Spe	$F1$	AUC
GNN+Node2vec	79.234	79.390	67.500	79.094	78.078
GNN+Node2vec +BAN	81.142	81.232	72.458	80.404	80.232

Table 5. Ablation study results for the GFC module.

Module	Acc	Sen	Spe	*F*1	AUC
GNN+Node2vec+CSegCos	81.250	81.546	74.782	80.136	80.476
GNN+Node2vec+CFcCos	79.372	80.468	76.032	79.688	79.026
GNN+Node2vec+NSegCos	78.748	79.360	70.000	79.490	78.050
GNN+Node2vec+NFcCos	78.746	79.418	73.750	78.712	78.538
GNN+Node2vec+NInterCos	77.496	78.482	70.000	78.072	77.074
GNN+Node2vec+GFC(CCroCos)+BAN	84.375	87.500	78.750	85.714	83.097

channels; and "*N*" denotes cosine similarity across nodes. The results showed that channel-wise cosine similarity outperformed node-wise similarity. Among them, the channel-cropped cosine similarity method (CCroCos) achieved the best performance and was adopted as the implementation of the GFC module in this study.

3.3. *Analysis of significant brain regions and their features*

The UGrad-CAM[56] was used to visualize the salient brain regions. As shown in Fig. 4, highweight regions were mainly distributed in the temporooccipital cortex and sensorimotorrelated areas, including the lingual gyrus, temporal fusiform cortex, frontal orbital cortex, opercular regions, planum polare, superior temporal gyrus, precentral gyrus, and superior parietal lobule. These regions showed a diffuse cortical distribution with evident hemispheric laterality.

The top 20 important brain regions identified using the Harvard-Oxford atlas were mapped onto the Yeo 7 functional networks (Table 6), enabling interpretation of the model-derived regions within established functional network architecture relevant to schizophrenia.

Saliency-based feature analysis (Fig. 5, left) showed that cortical thickness, global FCD, mFOCA, and ReHo had strong contributions to the model output. Statistical analyses further revealed significant alterations in these features within high-weight regions in patients compared with controls (Fig. 5, right). Overlap between the two analyses — such as for cortical thickness and ReHo — highlights their potential pathophysiological relevance.

3.4. *Prediction analysis of symptom severity in patients with schizophrenia*

According to the modelfitting results, the predictions for general and negative symptoms showed low error (small MSE, RMSE, and MAE, with MAPE around 10%) and strong positive correlations with the true values (correlation coefficients of 0.7195 and 0.6984, both with significant *P* values), indicating good predictive performance for these symptom domains. In contrast, the prediction of positive symptoms showed large deviations, with a markedly higher error (MAPE of 42.39%) and a nonsignificant

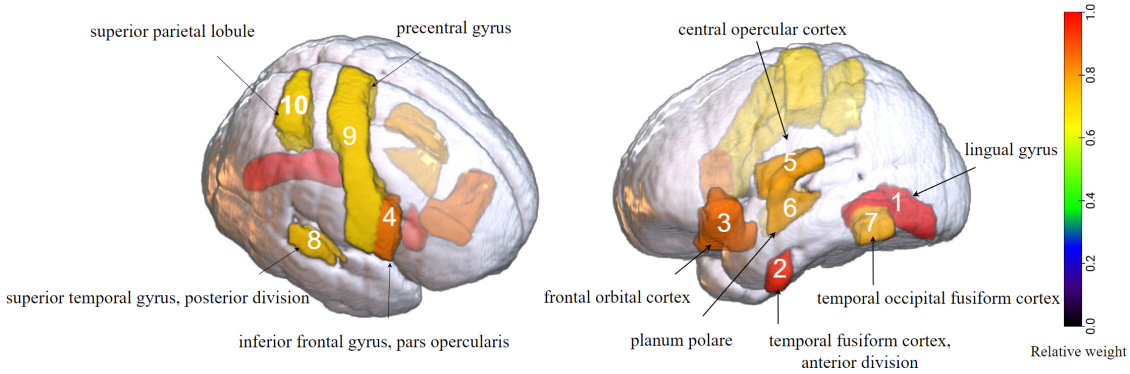

Fig. 4. Visualization of the top 10 most significant brain regions.

Table 6. Top 20 brain regions identified by the UGradCAM method.

HOA brain area name	Yeo 7 network	Relative weight
Lingual gyrus (LG.L)	Visual	1.0000
Temporal fusiform cortex, anterior division (TFusC-ant.L)	Ventral attention	0.9057
Frontal orbital cortex (FOC.L)	Limbic	0.6516
Inferior frontal gyrus, pars opercularis (IFGop.L)	Frontoparietal	0.6131
Central opercular cortex (COC.L)	Somatomotor	0.4721
Planum polare (PP.L)	N.A	0.4598
Temporal occipital fusiform cortex (TOFusC.R)	Ventral attention	0.4422
Superior temporal gyrus, posterior division (STGp.R)	Default mode	0.3367
Precentral gyrus (PreCG.R)	Somatomotor	0.2650
Superior parietal lobule (SPL.R)	Dorsal attention	0.2594
Parahippocampal gyrus, anterior division (PHGa.L)	Limbic	0.2554
Temporal fusiform cortex, posterior division (TFusC-post.L)	Ventral attention	0.2552
Insular cortex (INS.R)	N.A (Salience)	0.1414
Postcentral gyrus (PoCG.R)	Somatomotor	0.1161
Middle temporal gyrus, temporooccipital part (MTGto.R)	Default mode	0.0995
Middle temporal gyrus, anterior division (MTGa.R)	Default mode	0.0856
Supracalcarine cortex (SCC.L)	Visual	0.0813
Superior temporal gyrus, anterior division (STGa.R)	Default mode	0.0176
Heschl's gyrus (includes H1 and H2) (HG.L)	N.A	0.0061
Middle frontal gyrus (MFG.R)	Frontoparietal	0.0000

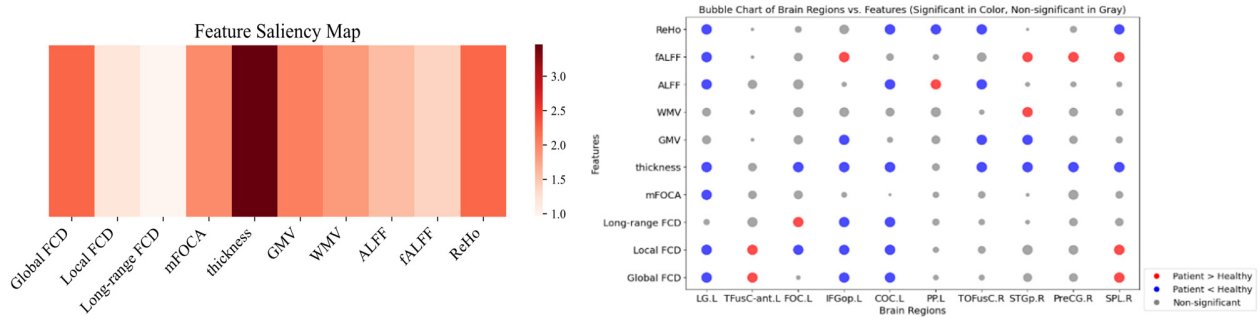

Fig. 5. (Color online) Saliency-based feature gradient heatmap (left) and bubble plot of significant brainregion features between the HC and patient groups (right). Bubble size indicates feature significance. Gray bubbles denote no significant group difference. Red bubbles indicate higher feature values in the patient group compared with HC, while blue bubbles indicate the opposite.

negative correlation coefficient (−0.3520), suggesting that the model was unable to effectively capture the variability of positive symptoms (Table 7).

4. Discussion

Inspired by GNNs, this study proposed C-GNN, a deep learning model that integrates multimodal MRI features. Based on the graph embedding module, the model enables the extraction of high-dimensional features from white matter connectivity. The BAN and GFC modules were designed to achieve node and feature selection, respectively, effectively capturing features on relatively small sample sizes and distinguishing schizophrenia patients from HCs with an accuracy of 84.375%. Ablation experiments gave evidence for the effectiveness of the three modules. Based on model visualization, nodes (brain regions) with significant importance for classification were identified, indicating that the intrinsic features of these brain regions and their information interaction patterns with other brain regions exhibit substantial disease effects. Furthermore, statistical analysis revealed the pattern of feature alterations in core

Table 7. Performance of scale prediction models based on significant subnetworks.

Symptom category	MSE	RMSE	MAE	MAPE	R	P
General symptoms	8.9019	2.9836	2.7076	0.1004	0.7195	0.0125
Positive symptoms	38.9161	6.2383	5.3453	0.4239	−0.3520	0.2884
Negative symptoms	10.5072	3.2415	2.3962	0.1104	0.6984	0.0168

impaired brain regions, and predictive analysis was applied to explore the relationship between subnetwork features formed by these brain regions and clinical manifestations of the disease.

4.1. *Module effectiveness*

This study systematically validated the contribution of each module through ablation experiments. Incorporating Node2vec to embed the white matter connectome as edge features enhanced the representation of global topological structure. In the branched attention network, max and average pooling, together with a multilayer perceptron, generated cross-channel attention weights that directed the model toward informative brain regions and feature channels. The GFC module further refined channel learning via channeldifferentiation scores. Among the tested strategies, the cosinesimilarity-based channel-cropped method yielded the best performance by reducing redundancy and limiting overfitting. Overall, the ablation results confirmed the essential contribution of each module to improving model performance and robustness.

4.2. *Significant brain regions revealed by C-GNN model*

The DMN demonstrated the highest frequency of involvement, suggesting its potential central role in the pathogenesis of schizophrenia. This result is consistent with previous research demonstrating the prevalence of DMN dysfunction in schizophrenia.[57,58] The ventral attention network and somatomotor network were also highly represented, reflecting potential abnormalities in attention regulation and sensory-motor integration in schizophrenia.[59,60]

Frontal regions (e.g. Frontal Orbital Cortex, Inferior Frontal Gyrus): primarily manifested decreased cortical thickness and local FCD, with increases in some indicators (e.g. long-range FCD, fALFF). This pattern suggests impaired local integration in the frontal lobe, potentially accompanied by abnormal enhancement of long-range functional pathways. Given the extensive involvement of the frontal lobe in cognitive control and language processing, this pattern may be associated with executive dysfunction, disorganized thinking, and speech abnormalities in patients with schizophrenia. Notably, our model identified the frontoorbital cortex and the inferior frontal gyrus as significant regions, consistent with previous studies showing that schizophrenia patients with treatment-resistant auditory verbal hallucinations (SCH-H) exhibited abnormal cortical folding in the frontoorbital cortex[61] and first-episode treatment-naïve patients with schizophrenia (FES) exhibited significantly reduced GMC in the inferior frontal gyrus.[62]

Temporal regions (e.g. superior Temporal Gyrus, Planum Polare, Temporal Fusiform Cortex, Anterior Division): In these regions, structural atrophy coexisted with increased functional activity. Specifically, the Temporal Fusiform Cortex, anterior division, showed abnormally increased function, suggesting possible abnormalities in social perception and semantic processing. Our model further supported the involvement of the superior temporal gyrus and the fusiform gyrus, two regions that had been repeatedly implicated in schizophrenia.[63,64]

The parietal area (superior parietal lobule) showed decreased cortical thickness and ReHo, but increased FCD and fALFF. This suggests a network imbalance in the parietal lobe involved in multimodal integration and attention, potentially leading to abnormalities in perceptual and attentional processing.[65] Although less explored in the schizophrenia literature, our findings suggested that the superior parietal lobule may hold potential for research.

Occipital/visual cortex (Lingual Gyrus, Temporal Occipital Fusiform Cortex): The lingual gyrus showed significant decreases in nearly all features, potentially related to visual processing deficits and hallucinations. The fusiform gyrus at the

occipito-temporal junction showed both structural and functional decreases, further supporting the idea of impaired visual semantic processing.[66] Previous studies have also reported reduced GMV in the fusiform gyrus and lingual gyrus in patients with first-episode schizophrenia.[67] The similar changes we observed in chronic patients suggest that these brain regions may be persistently affected during the course of the disease, supporting their important role in the pathogenesis of schizophrenia.

Insular cortex (Central Opercular Cortex): Multiple indicators were decreased, suggesting severe impairment in speech perception and integration, potentially explaining auditory hallucinations and language-related symptoms.

Motor cortex (Precentral Gyrus): Decreased cortical thickness but increased fALFF suggest coexisting structural damage and excessive spontaneous activity, potentially related to the patient's motor abnormalities or medication sensitivity.

Overall, patients with schizophrenia exhibit widespread abnormalities across multiple brain regions and features. These abnormalities manifest themselves in both significant decreases in structural measures (such as cortical thickness and GMV) and abnormal increases or decreases in functional measures (such as FCD and Alff). Cortical thickness decreased in nearly all brain regions, consistent with our previous research using sMRI to investigate cortical atrophy during schizophrenia progression.[68] Some brain regions recurred across different characteristic dimensions, suggesting that these regions may be core affected nodes of the disease (such as the lingual gyrus, central opercular cortex, inferior frontal gyrus, and pars opercularis). Furthermore, the pattern of structural decreases and functional increases observed in multiple brain regions may reflect potential compensatory mechanisms or overactivation of neural networks.

4.3. *Limitations*

Although our model provides some visual insights and biologically meaningful interpretations, it has several limitations.

First, the majority of patients with schizophrenia included in this study were taking antipsychotic medications during the imaging period. Medication may suppress positive symptoms while leaving prominent negative symptoms, and the high heterogeneity and temporal fluctuation of positive symptoms further complicate their prediction. Medicationrelated alterations in brain structure and function may also confound imaging–pathophysiology relationships, and such effects cannot be fully excluded.

Second, the study employed a cross-sectional design, which limits causal inference regarding the relationship between identified neuroimaging features and disease progression.

Third, the dataset was derived from a specific cohort with a modest sample size, and thus, the generalizability of the model to broader populations requires further validation.

5. Conclusion

This study developed a C-GNN model using multimodal features that achieved 84.37% accuracy in the detection of schizophrenia patients. The model incorporated novel BAN and GFC modules, demonstrating superior efficiency and robustness under limited sample conditions. Subsequent model analysis elucidated disease-related brain nodes and their distinctive characteristics. Nodelevel functional metrics (FCD, ALFF, ReHo) and cortical thickness exhibited significant abnormalities in patients, reflecting functional and structural disruptions. Several key regions were highlighted as critical nodes potentially linked to altered language, memory, perception, and social cognition. Previously understudied regions, such as planum polare and central opercular cortex, contributed strongly to classification, indicating their potential as novel biomarkers for schizophrenia.

Acknowledgments

This research was financially supported by the National Key R&D Program of China, (Grant No. 2024YFE0215100), the National Natural Science Foundation of China (Grant Nos. 62571106, 62401124, 82371560, and 62003058), the Natural Science Foundation of Sichuan Province (Grant Nos. 2023NSFSC0037 and 2023NSFSC0482), and the Project of Science and Technology Department of Sichuan Province (Grant No. 2024YFG0012).

The authors declare no conflicts of interest, financial or otherwise.

Appendix A

Data Preprocessing

Since multimodal data require preprocessing and feature extraction, several software packages were used, including fMRIPrep, Statistical Parametric Mapping (SPM), FMRIB Software Library (FSL), Neuroscience Information Toolbox (NIT), and the Resting-State fMRI Data Analysis Toolkit (REST). Specifically:

Structure MRI: FreeSurfer 7.3.2 was used for anatomical MRI processing. The "reconall" pipeline performed motion correction, intensity normalization, brain inflation, spherical mapping, and cortical parcellation. After preprocessing, vertex-wise cortical thickness and voxel-wise gray and white matter volumes were extracted and used for subsequent graph construction.

Functional MRI: Restingstate fMRI data were preprocessed using SPM12 and fMRIPrep (21.0.0). The first five frames were removed, followed by slicetiming and headmotion correction. Confound regressors included motion parameters, whitematter and CSF signals, linear drift, and global signals. fMRI data were aligned to the structural space for surface smoothing and then registered to MNI space. Scans with framewise displacement $> 2\,\text{mm}$ or rotation $> 1^\circ$ were excluded.

Functional features were extracted according to the HarvardOxford atlas. ALFF, fALFF, and ReHo were calculated using REST, while functional connectivity density (FCD) and four-dimensional (spatiotemporal) consistency of local neural activities (FOCA) were computed using NIT. All features were averaged within each region and used as node attributes in the graph neural network.

Diffusion MRI: Diffusion MRI data (UESTC dataset) were preprocessed using the FSL pipeline (v6.0.4) following our previous procedures. Steps included correction for eddy currents, motion, and susceptibility distortions; rigid alignment of the b0 image to the structural image using FLIRT; nonlinear registration to MNI152 space with FNIRT; and computation of forward and reverse warp fields between diffusion and structural spaces. Diffusion parameters were estimated voxelwise using MCMC sampling, modeling up to two fiber populations after 2000 iterations. Quality control included inspection of structural and b0 images and registration outputs. Data were excluded if the signaltonoise ratio of structural or b0 images was < 800 or if framewise displacement exceeded 2 mm.

Table A.1. List of preprocessing software tools.

Software	Main function
SPM12	Statistical analysis
fMRIPrep	Standard fMRI automated preprocessing
FSL	Tissue segmentation, dMRI preprocessing, and probabilistic fiber tracking
FreeSurfer	Cortical reconstruction, volume extraction, and cortical thickness extraction
REST	Calculation of ALFF and fALFF
NIT	Calculation of functional connectivity metrics such as FCD, FOCA, and ReHo

Table A.2. Analysis of learning rate selection for the CCNN model; the best result is highlighted in bold.

Lr	Batch	Acc	Sen	Spe	$F1$	AUC
0.0001	32	74.500	75.000	56.250	78.950	75.000
0.00001	32	79.372	80.685	74.376	80.214	78.746
0.0000085	**32**	**84.375**	**87.500**	**78.750**	**85.714**	**83.097**
0.000005	32	81.250	81.876	79.998	80.867	80.937
0.000001	32	69.376	70.002	76.875	76.907	69.376

ORCID

Jinnan Gong https://orcid.org/0000-0002-9908-3517
Roberto Rodriguez-Labrada https://orcid.org/0000-0003-3193-7683
Dezhong Yao https://orcid.org/0000-0002-8042-879X
Sisi Jiang https://orcid.org/0000-0002-7430-9639
Cheng Luo https://orcid.org/0000-0003-0524-5886

References

1. M. Fusté, A. Pauls, A. Worker, A. A. T. S. Reinders, A. Simmons, S. C. R. Williams, J. M. Haro, K. Hazelgrove, S. Pawlby, S. Conroy, C. Vecchio, G. Seneviratne, C. M. Pariante, M. A. Mehta and P. Dazzan, Brain structure in women at risk of postpartum psychosis: An MRI study, *Transl. Psychiatry* **7**(12) (2017) 1286, doi: 10.1038/s41398-017-0003-8.
2. Y. X. Bai, J. X. Luo, D. Peng, J. J. Sun, Y. F. Gao, L. X. Hao, B. G. Tong, X. M. He, J. Y. Luo, Z. H. Liang and F. Yang, Brain network functional connectivity changes in long illness duration chronic schizophrenia, *Front. Psychiatry* **15** (2024) 1423008, doi: 10.3389/fpsyt.2024.1423008.
3. H. Mohammadi and W. Karwowski, Graph neural networks in brain connectivity studies: Methods, challenges, and future directions, *Brain Sci.* **15**(1) (2025) 17, doi: 10.3390/brainsci15010017.
4. Y. Jiao, K. Zhao, X. Wei, N. B. Carlisle, C. J. Keller, D. J. Oathes, G. A. Fonzo and Y. Zhang, Deep graph learning of multimodal brain networks defines treatment-predictive signatures in major depression, *Mol. Psychiatry* **30**(9) (2025) 3963–3974, doi: 10.1038/s41380-025-02974-6.
5. B. Masoudi, S. Daneshvar and S. N. Razavi, A multimodal fusion of features method based on deep belief networks to diagnosis schizophrenia disease, *Int. J. Wavelets Multiresolution Inf. Process.* **19**(3) (2021) 20500885, doi: 10.1142/S0219691320500885.
6. H. Pei, S. Jiang, M. Liu, G. Ye, Y. Qin, Y. Liu, M. Duan, D. Yao and C. Luo, Simultaneous EEG-fMRI investigation of rhythm-dependent thalamo-cortical circuits alteration in schizophrenia, *Int. J. Neural Syst.* **34**(7) (2024) 2450031, doi: 10.1142/S012906572450031X.
7. B. G. Nelson, D. S. Bassett, J. Camchong, E. T. Bullmore and K. O. Lim, Comparison of large-scale human brain functional and anatomical networks in schizophrenia, *Neuroimage Clin.* **15** (2017) 439–448, doi: 10.1016/j.nicl.2017.05.007.
8. J. E. Arco, A. Ortiz, N. J. Gallego-Molina, J. M. Górriz and J. Ramírez, Enhancing multimodal patterns in neuroimaging by siamese neural networks with self-attention mechanism, *Int. J. Neural Syst.* **33** (4) (2023) 2350019, doi: 10.1142/S0129065723500193.
9. L. Zhang, C. Zhang, H. Yan, Y. Han, C. Xu, J. Liang, R. Li, N. Chen, W. Liang, W. Huang, G. Xie and W. Guo, Changes in degree centrality and its associated genes: A longitudinal study of patients with schizophrenia undergoing pharmacological treatment, *Schizophr. Res.* **277** (2025) 130–139, doi: 10.1016/j.schres.2025.03.009.
10. M. L. Hu, X. F. Zong, J. J. Mann, J. J. Zheng, Y. H. Liao, Z. C. Li, Y. He, X. G. Chen and J. S. Tang, A review of the functional and anatomical default mode network in schizophrenia, *Neurosci. Bull.* **33**(1) (2017) 73–84, doi: 10.1007/s12264-016-0090-1.
11. J. Kambeitz, L. Kambeitz-Ilankovic, C. Cabral, D. B. Dwyer, V. D. Calhoun, M. P. Van Den Heuvel, P. Falkai, N. Koutsouleris and B. Malchow, Aberrant functional whole-brain network architecture in patients with schizophrenia: A meta-analysis, *Schizophr. Bull.* **42**(suppl 1) (2016) S13–S21, doi: 10.1093/schbul/sbv174.
12. J. Zhu, Y. Qian, B. Zhang, X. Li, Y. Bai, X. Li and Y. Yu, Abnormal synchronization of functional and structural networks in schizophrenia, *Brain Imaging Behav.* **14**(6) (2020) 2232–2241, doi: 10.1007/s11682-019-00175-8.
13. Y. L. E. Chan, S. J. Tsai, Y. Chern and A. C. Yang, Exploring the role of hub and network dysfunction in brain connectomes of schizophrenia using functional magnetic resonance imaging, *Front. Psychiatry* **14** (2024) 1305359, doi: 10.3389/fpsyt.2023.1305359.
14. J. Zhou, G. Cui, S. Hu, Z. Zhang, C. Yang, Z. Liu, L. Wang, C. Li and M. Sun, Graph neural networks: A review of methods and applications, *AI Open* **1** (2020) 57–81, doi: 10.1016/j.aiopen.2021.01.001.
15. K. Zheng, S. Yu, L. Chen, L. Dang and B. Chen, BPI-GNN: Interpretable brain network-based psychiatric diagnosis and subtyping, *NeuroImage* **292** (2024) 120594, doi: 10.1016/j.neuroimage.2024.120594.
16. B. Thapaliya, E. Akbas, J. Chen, R. Sapkota, B. Ray, P. Suresh, V. Calhoun and J. Liu, Brain networks and intelligence: A graph neural network based approach to resting state fMRI data, *Med. Image Anal.* **101** (2025) 103433.
17. X. Zeng, J. Gong, W. Li and Z. Yang, Knowledge-driven multi-graph convolutional network for brain network analysis and potential biomarker discovery, *Med. Image Anal.* **99** (2025) 103368, doi: 10.1016/j.media.2024.103368.
18. M. E. Shenton, H. M. Hamoda, J. S. Schneiderman, S. Bouix, O. Pasternak, Y. Rathi, M. A. Vu, M. P. Purohit, K. Helmer, I. Koerte, A. P. Lin, C. F. Westin, R. Kikinis, M. Kubicki, R. A. Stern and R. Zafonte, A review of magnetic resonance imaging and diffusion tensor imaging findings in mild traumatic brain injury, *Brain Imaging Behav.* **6**(2) (2012) 137–192, doi: 10.1007/s11682-012-9156-5.
19. D. Sadeghi, A. Shoeibi, N. Ghassemi, P. Moridian, A. Khadem, R. Alizadehsani, M. Teshnehlab, J. M. Gorriz, F. Khozeimeh, Y. D. Zhang, S. Nahavandi and U. R. Acharya, An overview of artificial intelligence

techniques for diagnosis of schizophrenia based on magnetic resonance imaging modalities: Methods, challenges, and future works, *Comput. Biol. Med.* **146** (2022) 105554, doi: 10.1016/j.compbiomed.2022.105554.

20. C. M. W. Tax, M. Bastiani, J. Veraart, E. Garyfallidis and M. Okan Irfanoglu, What's new and what's next in diffusion MRI preprocessing, *NeuroImage* **249** (2022) 118830, doi: 10.1016/j.neuroimage.2021.118830.
21. H. P. Müller and J. Kassubek, Toward diffusion tensor imaging as a biomarker in neurodegenerative diseases: Technical considerations to optimize recordings and data processing, *Front. Hum. Neurosci.* **18** (2024) 1378896, doi: 10.3389/fnhum.2024.1378896.
22. L. Dong, C. Luo, W. Cao, R. Zhang, J. Gong, D. Gong and D. Yao, Spatiotemporal consistency of local neural activities: A new imaging measure for functional MRI data, *J. Magn. Reson. Imaging* **42**(3) (2015) 729–736, doi: 10.1002/jmri.24831.
23. D. Tomasi and N. D. Volkow, Functional connectivity density mapping, *Proc. Natl. Acad. Sci. USA* **107**(21) (2010) 9885–9890, doi: 10.1073/pnas.1001414107.
24. A. M. Winkler, P. Kochunov, J. Blangero, L. Almasy, K. Zilles, P. T. Fox, R. Duggirala and D. C. Glahn, Cortical thickness or grey matter volume? The importance of selecting the phenotype for imaging genetics studies, *NeuroImage* **53**(3) (2010) 1135–1146, doi: 10.1016/j.neuroimage.2009.12.028.
25. T. E. J. Behrens, H. J. Berg, S. Jbabdi, M. F. S. Rushworth and M. W. Woolrich, Probabilistic diffusion tractography with multiple fibre orientations: What can we gain?, *NeuroImage* **34**(1) (2007) 144–155, doi: 10.1016/j.neuroimage.2006.09.018.
26. K. S. Kendler, S. H. Aggen, G. P. Knudsen, E. Røysamb, M. C. Neale and T. Reichborn-Kjennerud, The structure of genetic and environmental risk factors for syndromal and subsyndromal common DSM-IV axis I and all axis II disorders, *Am. J. Psychiatry* **168**(1) (2011) 29–39, doi: 10.1176/appi.ajp.2010.10030340.
27. V. Peralta and M. Cuesta, Psychometric properties of the positive and negative syndrome scale (PANSS) in schizophrenia, *Psychiatry Res.* **53** (1994) 31–40, doi: 10.1016/0165-1781(94)90093-0.
28. L. Clifford, S. Crabb, D. Turnbull, L. Hahn and C. Galletly, A qualitative study of medication adherence amongst people with schizophrenia, *Arch. Psychiatr. Nurs.* **34**(4) (2020) 194–199, doi: 10.1016/j.apnu.2020.06.002.
29. X. W. Song, Z. Y. Dong, X. Y. Long, S. F. Li, X. N. Zuo, C. Z. Zhu, Y. He, C. G. Yan and Y. F. Zang, REST: A toolkit for resting-state functional magnetic resonance imaging data processing, *PLoS One* **6**(9) (2011) e25031, doi: 10.1371/journal.pone.0025031.
30. R. Maffulli, M. A. Casal, M. Celotto, S. Zucca, H. Safaai, T. Fellin and S. Panzeri, NIT: An open-source tool for information theoretic analysis of neural population data, *bioRxiv* (2022), doi: 10.1101/2022.12.11.519966.
31. B. Fischl, FreeSurfer, *NeuroImage* **62**(2) (2012) 774–781, doi: 10.1016/j.neuroimage.2012.01.021.
32. G. Flandin and K. J. Friston, Statistical parametric mapping (SPM), *Scholarpedia* **3**(4) (2008) 6232, doi: 10.4249/scholarpedia.6232.
33. G. Rosenthal, F. Váša, A. Griffa, P. Hagmann, E. Amico, J. Goñi, G. Avidan and O. Sporns, Mapping higher-order relations between brain structure and function with embedded vector representations of connectomes, *Nat. Commun.* **9**(1) (2018) 2178, doi: 10.1038/s41467-018-04614-w.
34. A. Bundy and L. Wallen, Breadth-first search, in *Catalogue of Artificial Intelligence Tools*, eds. A. Bundy and L. Wallen (Springer, 1984), pp. 13–13, doi: 10.1007/978-3-642-96868-6_25.
35. J. H. Reif, Depth-first search is inherently sequential, *Inf. Process. Lett.* **20**(5) (1985) 229–234, doi: 10.1016/0020-0190(85)90024-9.
36. X. Rong, word2vec parameter learning explained, preprint (2016), arXiv:1411.2738.
37. M. Hassanin, S. Anwar, I. Radwan, F. S. Khan and A. Mian, Visual attention methods in deep learning: An in-depth survey, *Inf. Fusion* **108** (2024) 102417, doi: 10.1016/j.inffus.2024.102417.
38. S. Woo, J. Park, J. Y. Lee and I. S. Kweon, CBAM: Convolutional block attention module, in *Computer Vision — ECCV 2018*, Vol. 11211, Lecture Notes in Computer Science, eds. V. Ferrari, M. Hebert, C. Sminchisescu and Y. Weiss (Springer, 2018), pp. 3–19, doi: 10.1007/978-3-030-01234-2_1.
39. Q. Wang, B. Wu, P. Zhu, P. Li, W. Zuo and Q. Hu, ECA-Net: Efficient channel attention for deep convolutional neural networks, (2020), https://openaccess.thecvf.com/content_CVPR_2020/html/Wang_ECA-Net_Efficient_Channel_Attention_for_Deep_Convolutional_Neural_Networks_CVPR_2020_paper.html.
40. Y. S. Jhang, S. T. Wang, M. H. Sheu, S. H. Wang and S. C. Lai, Channel-wise average pooling and 1D pixel-shuffle denoising autoencoder for electrode motion artifact removal in ECG, *Appl. Sci.* **12**(14) (2022) 6957, doi: 10.3390/app12146957.
41. J. Hu, L. Shen, S. Albanie, G. Sun and E. Wu, Squeeze-and-excitation networks, preprint (2019), arXiv:1709.01507.
42. Z. Qin, P. Zhang, F. Wu and X. Li, FcaNet: Frequency channel attention networks, (2021), https://openaccess.thecvf.com/content/ICCV2021/html/Qin_FcaNet_Frequency_Channel_Attention_Networks_ICCV_2021_paper.html.
43. J. Xia, N. Chen and A. Qiu, Multi-level and joint attention networks on brain functional connectivity for cross-cognitive prediction, *Med. Image Anal.* **90** (2023) 102921, doi: 10.1016/j.media.2023.102921.
44. W. Fan, H. Bo, Y. Lin, Y. Xing, W. Liu, N. Lepora and D. Zhang, Graph neural networks for interpretable tactile sensing, in *27th Int. Conf. Automation and Computing (ICAC)* (IEEE, 2022), pp. 1–6.
45. P. E. Pope, S. Kolouri, M. Rostami, C. E. Martin and H. Hoffmann, Explainability methods for graph convolutional neural networks, in *2019 IEEE/CVF Conf.*

Computer Vision and Pattern Recognition (CVPR) (IEEE, 2019), pp. 10764–10773, doi: 10.1109/CVPR.2019.01103.
46. M. Defferrard, X. Bresson and P. Vandergheynst, Convolutional neural networks on graphs with fast localized spectral filtering, in *Advances in Neural Information Processing Systems* 29 (NIPS, 2016).
47. F. Murtagh, Multilayer perceptrons for classification and regression, *Neurocomputing* **2** (1991) 183–197, doi: 10.1016/0925-2312(91)90023-5.
48. T. N. Kipf and M. Welling, Semi-supervised classification with graph convolutional networks, preprint (2017), arXiv.1609.02907.
49. P. Veličković, G. Cucurull, A. Casanova, A. Romero, P. Liò and Y. Bengio, Graph attention networks, preprint (2018), arXiv.1710.10903.
50. W. Hamilton, Z. Ying and J. Leskovec, Inductive representation learning on large graphs, in *Advances in Neural Information Processing Systems*, Vol. 30 (Curran Associates Inc., 2017), https://proceedings.neurips.cc/paper/2017/hash/5dd9db5e033da9c6fb5ba83c7a7ebea9-Abstract.html.
51. F. Wu, T. Zhang, A. H. de Souza Jr., C. Fifty, T. Yu and K. Q. Weinberger, Simplifying graph convolutional networks, preprint (2019), arxiv.1902.07153.
52. H. Gao and S. Ji, Graph U-Nets, in *Proc. 36th Int. Conf. Machine Learning* (PMLR, 2019), pp. 2083–2092, https://proceedings.mlr.press/v97/gao19a.html.
53. G. Li, C. Xiong, A. Thabet and B. Ghanem, DeeperGCN: All you need to train deeper GCNs, (2020), arXiv.2006.07739.
54. M. Chen, Z. Wei, Z. Huang, B. Ding and Y. Li, Simple and deep graph convolutional networks, in *Proc. 37th Int. Conf. Machine Learning* (PMLR, 2020), pp. 1725–1735, https://proceedings.mlr.press/v119/chen20v.html.
55. S. A. Tailor, F. L. Opolka, P. Liò and N. D. Lane, Adaptive filters and aggregator fusion for efficient graph convolutions, preprint (2021), arXiv:2104.01481.
56. F. Ferri, M. Cannariato, L. Pallante, E. A. Zizzi and M. A. Deriu, Explainable machine learning and deep learning models for predicting TAS2R-bitter molecule interactions, preprint (2024), arXiv.2406.15039.
57. D. Sasabayashi, T. Takahashi, Y. Takayanagi, K. Nemoto, M. Ueno, A. Furuichi, Y. Higuchi, Y. Mizukami, H. Kobayashi, Y. Yuasa, K. Noguchi and M. Suzuki, Resting state hyperconnectivity of the default mode network in schizophrenia and clinical high-risk state for psychosis, *Cereb. Cortex* **33**(13) (2023) 8456–8464, doi: 10.1093/cercor/bhad131.
58. A. Kottaram, L. A. Johnston, L. Cocchi, E. P. Ganella, I. Everall, C. Pantelis, R. Kotagiri and A. Zalesky, Brain network dynamics in schizophrenia: Reduced dynamism of the default mode network, *Hum. Brain Mapp.* **40**(7) (2019) 2212–2228, doi: 10.1002/hbm.24519.
59. T. A. Hummer, M. G. Yung, J. Goñi, S. K. Conroy, M. M. Francis, N. F. Mehdiyoun and A. Breier, Functional network connectivity in early-stage schizophrenia, *Schizophr. Res.* **218** (2020) 107–115, doi: 10.1016/j.schres.2020.01.023.
60. A. M. Jimenez, J. Lee, J. K. Wynn, M. S. Cohen, S. A. Engel, D. C. Glahn, K. H. Nuechterlein, E. A. Reavis and M. F. Green, Abnormal ventral and dorsal attention network activity during single and dual target detection in schizophrenia, *Front. Psychol.* **7** (2016) 323, doi: 10.3389/fpsyg.2016.00323.
61. C. Núñez, C. Stephan-Otto, A. Roldán, E. M. Grasa, M. J. Escartí, E. J. Aguilar García-Iturrospe, G. García-Martí, M. de la Iglesia-Vaya, J. Nacher, M. J. Portella and I. Corripio, Orbitofrontal cortex hypergyrification in hallucinating schizophrenia patients: Surface ratio as a promising brain biomarker, *Eur. Neuropsychopharmacol.* **89** (2024) 47–55, doi: 10.1016/j.euroneuro.2024.09.006.
62. M. Li, W. Deng, Y. Li, L. Zhao, X. Ma, H. Yu, X. Li, Y. Meng, Q. Wang, X. Du, P. C. Sham, L. Palaniyappan and T. Li, Ameliorative patterns of grey matter in patients with first-episode and treatment-naïve schizophrenia, *Psychol. Med.* **53**(8) (2023) 3500–3510, doi: 10.1017/S0033291722000058.
63. S. Jung, J. H. Kim, N. O. Kang, G. Sung, Y. G. Ko, M. Bang, C. I. Park and S. H. Lee, Fusiform gyrus volume reduction associated with impaired facial expressed emotion recognition and emotional intensity recognition in patients with schizophrenia spectrum psychosis, *Psychiatry Res. Neuroimaging* **307** (2021) 111226, doi: 10.1016/j.pscychresns.2020.111226.
64. K. Ohi, Y. Matsuda, T. Shimada, T. Yasuyama, K. Oshima, K. Sawai, H. Kihara, Y. Nitta, H. Okubo, T. Uehara and Y. Kawasaki, Structural alterations of the superior temporal gyrus in schizophrenia: Detailed subregional differences, *Eur. Psychiatry* **35** (2016) 25–31, doi: 10.1016/j.eurpsy.2016.02.002.
65. S. Chieffi, C. R. Ilardi and A. Iavarone, Parietal lobe dysfunction in schizophrenia: A review, *Curr. Psychiatry Rev.* **14**(2) (2018) 71–83, doi: 10.2174/1573400514666180703150804.
66. Right lateral fusiform gyrus dysfunction during facial information processing in schizophrenia, *Biol. Psychiatry* **53**(12) (2003) 1099–1112, doi:10.1016/S0006-3223(02)01784-5.
67. M. Chang, F. Y. Womer, C. Bai, Q. Zhou, S. Wei, X. Jiang, H. Geng, Y. Zhou, Y. Tang and F. Wang, Voxel-based morphometry in individuals at genetic high risk for schizophrenia and patients with schizophrenia during their first episode of psychosis, *PLoS One* **11**(10) (2016) e0163749, doi: 10.1371/journal.pone.0163749.
68. Y. Jiang *et al.*, Neurostructural subgroup in 4291 individuals with schizophrenia identified using the subtype and stage inference algorithm, *Nat. Commun.* **15**(1) (2024) 5996, doi: 10.1038/s41467-024-50267-3.